ADVANCED ENERGY MATERIALS
www.advenergymat.de

Toward Green Processing of Perovskite Solar Cells: Protic Ionic Liquids Enable Water- and Alcohol-Based $MAPbI_3$ Precursors Inks for Slot-Die Coating

*Feray Ünlü, Alejandra Florez, Keely Dodd-Clements, Lennart Klaus Reb, Michael Götte, Matthias Grosch, Fengning Yang, Senol Öz, Florian Mathies, Sanjay Mathur, Daniel Ramírez, Franklin Jaramillo, and Eva Unger**

Halide perovskite solar cells are approaching commercialization, with solution processing emerging as a key method for large-scale production. This study introduces a significant advancement: using non-toxic solvents like water and alcohol in perovskite precursor inks facilitated by the protic ionic liquid methylammonium propionate (MAP). MAP effectively dissolves perovskite precursors such as lead acetate and methylammonium iodide, enabling the first stable water-based perovskite precursor ink suitable for one-step slot-die coating. This new ink formulation contrasts with conventional dimethylformamide (DMF) and dimethylsulfoxide (DMSO)-based inks, as evidenced by in-situ grazing incidence wide-angle X-ray scattering (GIWAXS), which revealed an intermediate-free liquid-to-solid transition. In-situ mass spectrometry also showed that organic molecules evaporate during annealing, resulting in a crystalline perovskite phase. Optimization of the solvent mixture to H_2O/IPA/MAP enabled successful slot-die coating, yielding perovskite solar cells with an efficiency of up to 10%. This eco-friendly ink reduces toxicity and environmental impact compared to DMF-based inks, offering a longer shelf life and the possibility of using the ink in ambient conditions. This pioneering work represents the first report of a water-based green ink formulation for one-step thin film coating at room-temperature conditions by slot-die coating, highlighting its potential for sustainable commercial applications.

1. Introduction

The structural and material flexibility of halide perovskites offers great opportunities for various fabrication techniques in large-scale manufacturing, such as inkjet printing, slot-die coating, blade-coating, roll-to-roll depositions, etc. However, all these techniques require solvents during processing that evaporate during the liquid-to-solid transition. In the initial phase of halide perovskite research, the selection of suitable solvents for perovskite precursors primarily relied on experimental trial-and-error methodologies, where solvents such as dimethyl formamide (DMF), dimethyl sulfoxide (DMSO) and *N*-methyl pyrrolidone (NMP) were found to have a favorable property to be used as solvents for lead halide (PbX_2) and organo-halide (AX) salts when preparing perovskite precursor inks.[1] The prerequisite for a suitable solvent is the capability to dissolve high concentrations of PbX_2 to deposit

F. Ünlü, K. Dodd-Clements, L. K. Reb, M. Götte, F. Mathies, E. Unger
HySPRINT Innovation Lab
Helmholtz-Zentrum Berlin für Materialen und Energie GmbH
Kekuléstraße 5, 12489 Berlin, Germany
E-mail: eva.unger@helmholtz-berlin.de

A. Florez, D. Ramírez, F. Jaramillo
Centro de Investigación
Innovación y Desarrollo de Materiales – CIDEMAT
Facultad de Ingeniería
Universidad de Antioquia UdeA
Calle 67 No. 52-21, Medellín 050010, Colombia

The ORCID identification number(s) for the author(s) of this article can be found under https://doi.org/10.1002/aenm.202403626

DOI: 10.1002/aenm.202403626

M. Grosch, S. Mathur
Inorganic and Materials Chemistry
University of Cologne
Greinstr. 6, 50939 Cologne, Germany

F. Yang
Department of Physics
University of Oxford
Clarendon Laboratory
Parks Road, Oxford OX1 3PU, UK

S. Öz
Solaveni GmbH
Siemensstr. 42, 59199 Bönen, Germany

E. Unger
Department of Chemistry
IRIS and CSMB
Humboldt University Berlin
Zum Großen Windkanal 2, 12489 Berlin, Germany

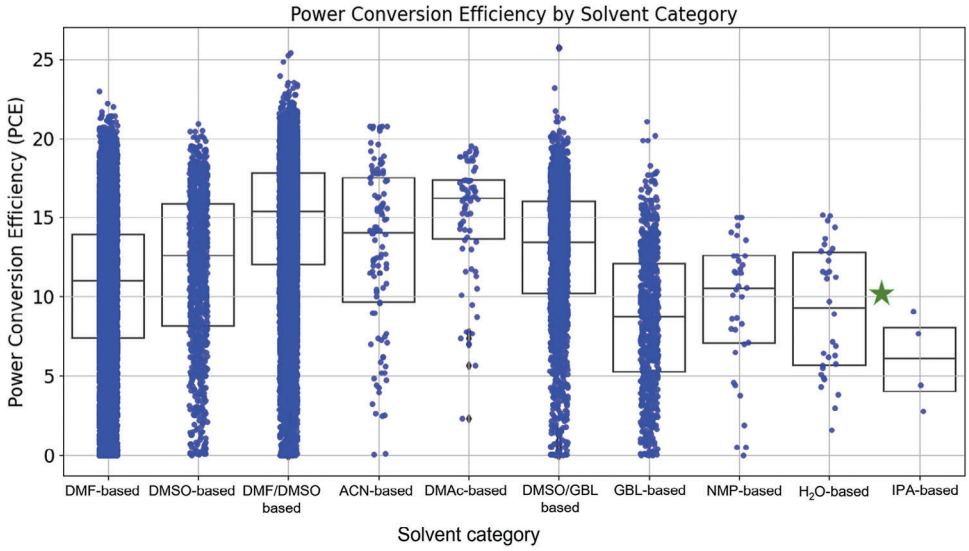

Figure 1. Overview of $MAPbI_3$-based perovskite solar cell efficiencies for the most used solvents in halide perovskite thin film processing, illustrated as the PCE plotted against the solvent category. This plot was generated from data available in *The Perovskite Database (perovskitedatabase.com)*, comprising data from >40 000 individual solar cells.[5] The power conversion efficiency achieved in this work from a water- and IPA-based ink achieved up to 10% (green star) using a single-step processing procedure.

the perovskite thin film with sufficient thickness (>300 nm) for adequate light harvesting. While the AX-salt dissolves in most solvents, finding a solvent that can dissolve the metal halide component is challenging. As reported in the literature, the formation of lead-halide-solvent coordination complexes[2,3] affects the solubility of perovskite precursors, where coordination, especially of excess halides, can lead to the dissolution of the PbI_2 framework and thus increase the solubility.[4]

Figure 1 shows the power conversion efficiencies (PCE) of $MAPbI_3$-based solar cells fabricated from common solvents and solvent mixtures in the published literature research over the last decade (extracted from *The Perovskite Database*).[5] As can be seen in Figure 1, the most common solvents are DMF, DMSO, and γ-butyrolactone (GBL) or a mixture thereof leading to best-reported efficiencies so far for single-junction methylammonium lead iodide ($MAPbI_3$) solar cells. Noticeably, these solvents dominantly used in halide perovskite processing are categorized as hazardous carcinogenic, mutagenic, and reprotoxic chemicals (CMR) chemicals. This poses a severe challenge for the large-scale manufacturing of halide perovskite materials. Therefore, it is a strategic necessity to develop inks with less toxic solvents and co-solvents for the deposition of thin perovskite films. Examples of solvents with low toxicity include γ-valerolactone (GVL), triethyl phosphate (protic) ionic liquids, alcohols such as ethanol and isopropanol (IPA), and water.[6]

For example, GVL enables the solution-based fabrication of high-quality $FAPbI_3$ solar cells, achieving an impressive power conversion efficiency (PCE) of up to 25.09%.[7] Water is the most sustainable, environmentally friendly solvent. In contrast to the concern about the adverse effects of water on the stability of perovskite materials, *Liu* et al. demonstrated that the presence of water in perovskite precursor did not negatively impact the perovskite thin film preparation process. A high water content (up to 25 vol%) was shown to enable perovskite's humidity tolerance during air fabrication. This was ascribed to the ability of water to prolong the film drying process, leading to the formation of perovskite thin films with large grain size and a reduced wettability of the thin film.[8] Overall, limited reports on water-based perovskite precursor solutions are typically only suitable for sequential deposition methods.[9–11]

In the search for green solvents for solution processing, protic ionic liquids (PILs), which are also called *room temperature molten salts*, have advantageous properties such as a non-volatile nature at room temperature or below, non-flammability, high thermal stability, as well as the ability to dissolve various organic and inorganic compounds compared to conventional solvents. Besides being used as additives to control the crystallization of perovskites,[12–15] PILs can also be used in combination with co-solvents. *Öz* et al. prepared a series of PILs based on methylammonium (MA, $CH_3NH_4^+$) and carboxylic acids to obtain methylammonium formate, (MAF), methylammonium acetate (MAA), and methylammonium propionate (MAP) and investigated these with co-solvents in solution processing of perovskites and demonstrated that the PILs, which have a strong hydrogen bonding, can dissolve the PbX_2 forming $MAPbX_3$ (X=Br, I) materials. The PILs can be mixed proportionately with other green solvents such as water, ethanol, isopropanol, and acetonitrile to tune the solvent viscosity. By using a MAP-DMSO-acetonitrile solvent mixture, a perovskite solar cell with a PCE of 15.46% based on $(MA_{0.15}FA_{0.85})Pb(I_{0.85}Br_{0.15})_3$ was obtained via a 2-step spin-coating method.[16] In a previous report, water- and MAP-based ink was used to fabricate $CsPbBr_3$-based perovskite fibers for electroluminescent applications, showing the high solubility of perovskite precursors in this solvent system.[17]

For commercialization purposes, the use of PILs in precursor inks is of high value due to their low toxicity, long shelf-life, and good processability, which reduces production costs and health risks. Slot-die coating was used as the deposition method of choice, which is widely employed in large-scale thin film PV fabrication and was also studied for perovskite solar cells.[18] The

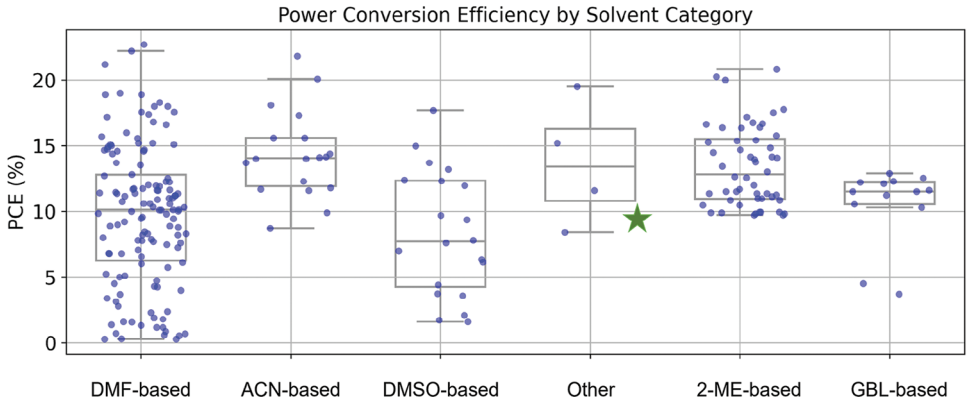

Figure 2. An overview of perovskite solar cell efficiencies for slot-die coated perovskite layers is illustrated as the PCE plotted against the solvent category. This plot was generated from data available in *The Perovskite Database (perovskitedatabase.com)*.[5]

advantage of slot-die coating is the scalability of the thin film processing, allowing the control of large-scale deposition, which is critical for thin film fabrication on an industrial scale. Moreover, it is a fast and more sustainable process as less ink is used during the thin film deposition than spin-coating, where a large amount of residual ink is flung off and wasted during spinning.

Figure 2 shows the solar cell data in the literature for slot-die-coated perovskite layers, which has been studied less than the spin-coating method. Also, the main solvent systems are still based on toxic solvents, including DMF, GBL, acetonitrile, and 2-methoxyethanol.

Only a few categorized under "other" contain less toxic solvents; for example, *Razaee* et al. demonstrate a roll-to-roll produced perovskite solar cells using up to 90 vol% ethanol combined with small amounts of acetonitrile.[19]

Although some water-based perovskite solar cell fabrications were shown in the literature, the reports only include multiple steps for the perovskite thin film formation.[42,43] However, incorporating multiple cycles into large-scale industrial production presents significant challenges. While single-step processes are relatively straightforward, given that the record solar cells are made this way,[44,45] the complexity of multiple steps increases the difficulty of maintaining precise control over the entire production process. Each additional deposition step requires careful synchronization across large areas, ensuring consistent thin-film morphology and homogeneity. This added complexity impacts time efficiency—slowing production and increasing energy consumption—and heightens the uncertainty in achieving reproducible PSCs, making scalability more challenging.[42] Furthermore, the cost of fabrication, which is not the main scope considered in this study, is an essential factor for the realization of commercial production of perovskite solar cells.[44] Stable, green, and one-step suitable perovskite inks will positively impact the cost factor of the whole fabrication process, leading to an overall sustainable emerging technology.

In this work, we have developed a green $MAPbI_3$ perovskite precursor ink with an extended shelf life for use in a single-step slot-die coating process, achieving PCEs up to 10%. We demonstrate the possibility of using alternative and non-toxic solvents such as water and isopropanol in combination with a protic ionic liquid and lead acetate as the lead precursor. Furthermore, we characterize the solution chemistry of the new precursor ink to rationalize the influence of solvents in the perovskite formation. Finally, we conduct a life cycle impact analysis – the newly formulated ink is "greener" than the standard $MAPbI_3$ DMF ink.

2. Results and Discussion

2.1. Solution Chemistry of Water-Based Perovskite Precursor Inks

In this work, methylammonium propionate (MAP, $[CH_3NH_3]^+[CH_3COO]^-$) was used as a protic ionic liquid and co-solvent to formulate water-based perovskite inks. MAP (**3**) was synthesized from methylamine (**1**) and propionic acid (**2**) through a simple Brønsted acid-base reaction (**Scheme 1**).

In the following paragraph, the process that leads to the final green ink formulation is described. The formulated 0.3 M $MAPbI_3$ precursor ink with PbI_2/CH_3NH_3I (1:1), H_2O/MAP was not stable due to the low solubility of the lead salts in water (PbI_2 0.63 g L^{-1} at 20 °C).[20] A clear solution was obtained after stirring at 60–70 °C; however, the lead salt precipitated after cooling to room temperature. To prevent the problem of reprecipitation of the lead salt upon cooling, lead acetate ($Pb(CH_3COO)_2$) was used instead since it has a better solubility in water (465 g L^{-1} at 20 °C).[20] In the next attempt, $Pb(CH_3COO)_2$ and methylammonium iodide (MAI) were dissolved in water in a 1:3 mol ratio, which did not succeed even at temperatures of 70 °C. Therefore, MAP was added as the co-solvent to achieve a precise and stable solution mixture of H_2O/MAP (2:3 v/v) with a solution concentration of 0.3 M (**Figure 3a**).

A volume ratio of 2:3 between H_2O and MAP was the highest amount of water possible to obtain a stable and clear perovskite

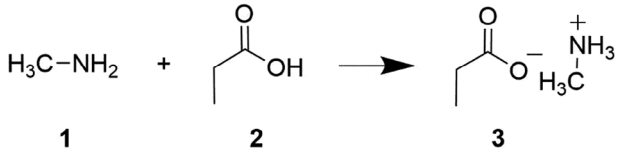

Scheme 1. Reaction scheme for the synthesis of the PIL methylammonium propionate (**3**) through the acid-base reaction of methylamine (**1**) and propionic acid (**2**).

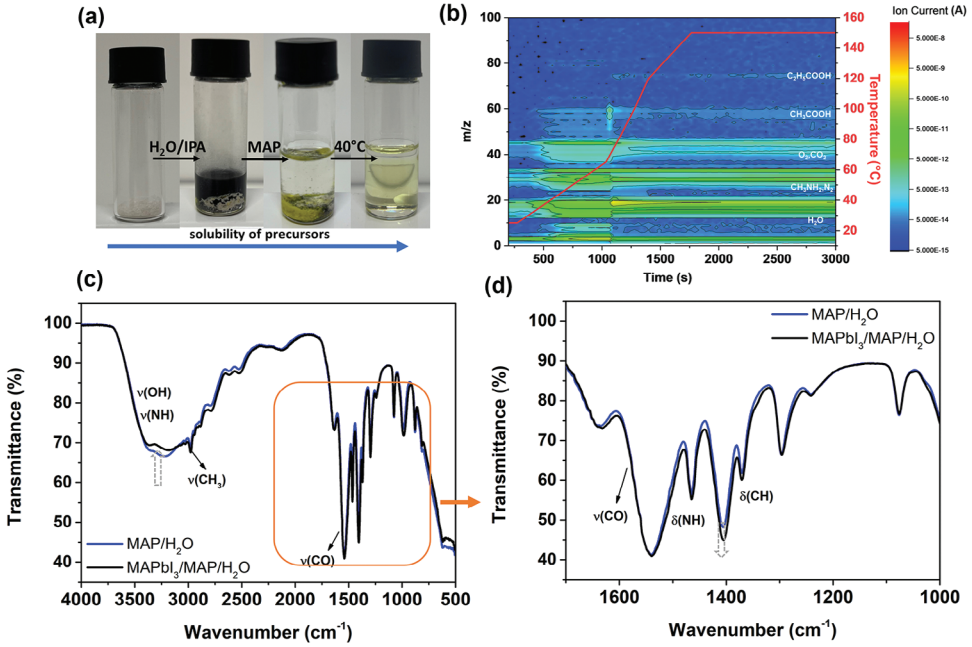

Figure 3. a) Picture of $MAPbI_3$ precursors in pure green solvents and the increase of solubility after the addition of the protic ionic liquid MAP; b) 2D Mass spectrum during the wet film annealing of the water-based $MAPbI_3$ ink plotted as a mass-to-charge ratio (m/z) over time (t). The intense m/z were assigned to the molecules listed on the right axis; the temperature ramp is also shown (red curve) c) FT-IR spectra of the 0.3 M perovskite precursor inks of $MAPbI_3$ precursors (black) in the solvent MAP/H_2O (3:2 v/v) solvent system (blue, neat solvent blend); d) zoom to the FT-IR spectrum range of C═O, ν(CO). The dashed arrows show the intensity changes between the spectra.

ink. The multi-component water-based ink consisting of organic molecules like propionate ($CH_3CH_2COO^-$, 5.76 mmol), acetate (CH_3COO^-, 0.32 mmol), and methylammonium ($CH_3NH_3^+$, 6.72 mmol) ions along with inorganic Pb^{2+} (0.32 mmol) and I^- (0.96 mmol), was analyzed during the annealing process resulting in the solid perovskite. For this purpose, a wet film was frozen in nitrogen and transferred into an ultrahigh vacuum micro chamber coupled with a mass spectrometer. The sample was annealed slowly (T═65 °C–150 °C) over time, and the released molecules were detected and plotted in Figure 3b (and Figure S1, Supporting information).

The most intense mass-to-charge (m/z) peaks were observed at m/z = 18, 28, 32, 44, 58, and 74, which can be assigned to water (H_2O or OH^-), methylamine (CH_3NH_2 (m/z ca. 32), methylammonium ($CH_3NH_3^+$, m/z ca. 33), components of air (N_2 m/z ca. 28, O_2 m/z ca. 32, and CO_2 m/z ca. 44), acetate (CH_3COO^-, m/z ca. 59) and propionate/propionic acid (C_2H_5COOH, m/z ca. 74). From these observations, a formation equation might be suggested as follows, where the perovskite is formed upon the release of the volatile organic molecules; acetic acid, propionic acid, and methylamine (Equation 1):

$$\begin{aligned} Pb(CH_3COO)_2 + 3CH_3NH_3I + 18[CH_3NH_3]\,[CH_3CH_2COO] \\ \text{solution stage aqueous} \rightarrow CH_3NH_3PbI_3 \\ +2\ CH_3COOH\uparrow +20\ CH_3NH_2\uparrow \\ +18\ CH_3CH_2COO\uparrow \end{aligned} \quad (1)$$

Fourier-transform infrared (FT-IR) spectra of the related water-based ink were recorded to investigate the role of water and PIL. Figure 2c shows no noticeable band shifts or changes compared to the neat H_2O/MAP solvent mixture (blue line). A slight intensity deviation can be observed in the broad OH/NH band region at 3000–3500 cm^{-1}; this might be caused by the disruption of the H-bonding upon adding $MAPbI_3$, leading to a slight decrease in the absorption band. No changes at the strongest absorption band at 1540 cm^{-1}, originating from the C═O stretching, is observed. Furthermore, in the fingerprint region 1400–500 cm^{-1}, a slight increase is seen in the δ(CH) band (Figure 3d), highly likely due to the increase of methyl groups upon adding $MAPbI_3$. In comparison, the FT-IR spectra of the water-based PIL inks are different from the "classical" $MAPbI_3$ inks in DMF and DMSO, where direct coordination can be inferred from the FTIR features as explained in the Supporting Information (Figures S2–S3, Supporting Information).

Thus, from these results, we either can conclude that there is no direct coordination to the Pb centers in the MAP/water-based inks, or another assumption might be that the relative molar amount of $MAPbI_3$ added to the ink is low compared to MAP, which suggests that the addition does not significantly alter the IR spectrum at first glance. The spectrum remains dominated by the H_2O/MAP interaction. The features may be too weak relative to the strong MAP and H_2O vibrations, causing them to be masked.

As only limited conclusions regarding the solvent-solvate interaction could be drawn from FT-IR measurements, nuclear magnetic resonance spectroscopy (NMR) measurements of the 0.3 M precursor inks were conducted using a deuterated D_2O/MAP

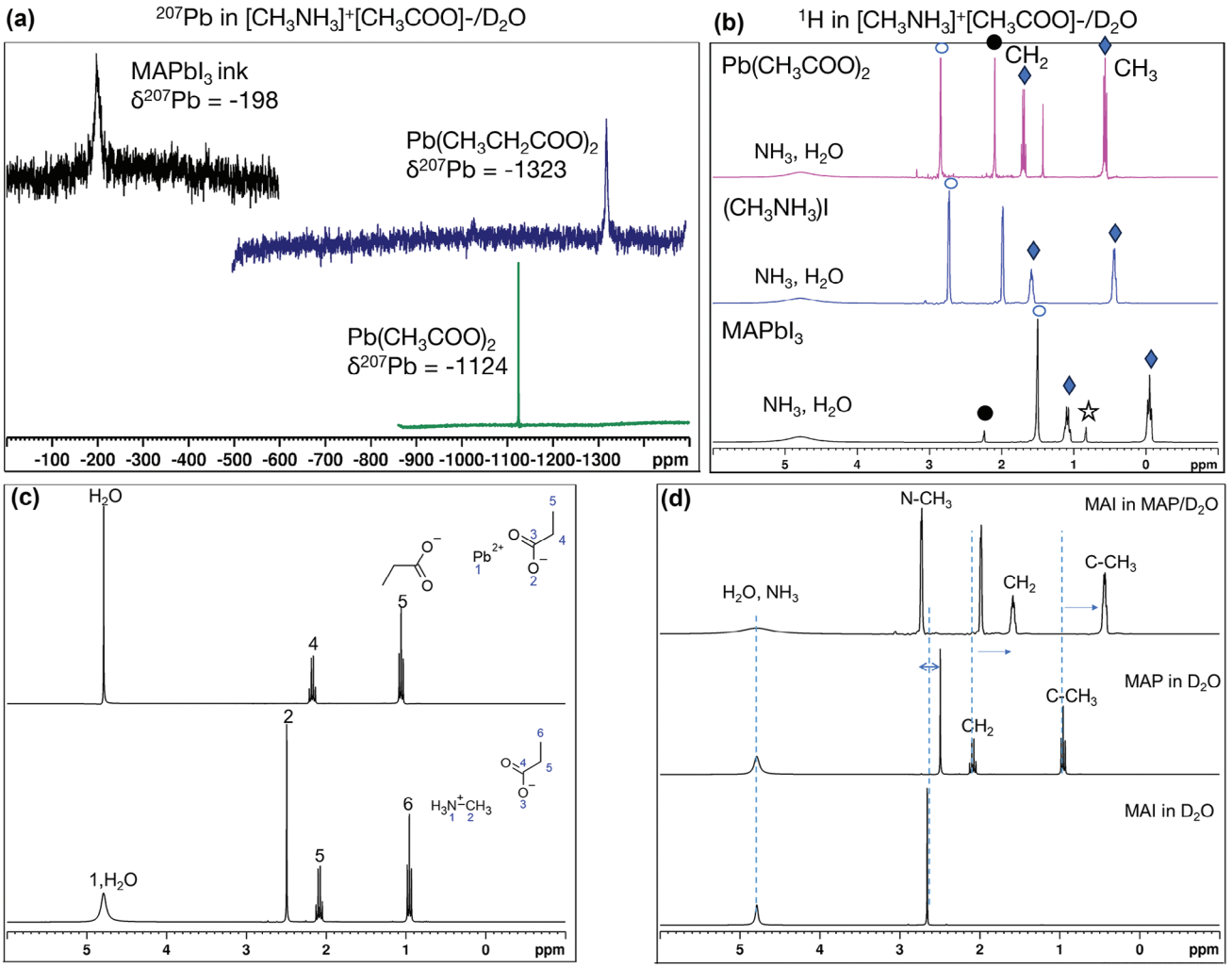

Figure 4. a) ^{207}Pb NMR spectra of 0.3 mol L^{-1} $MAPbI_3$ precursor ink (black) with the MAP/D_2O (3:2 v/v) solvent system compared to the neat solutions of lead propionate ($Pb(CH_3CH_2COO)_2$, blue) and lead acetate $Pb(CH_3COO)_2$ (green) in D_2O. Chemical shifts are reported on a ppm scale relative to $Pb(CH_3)_4$ ($\delta = 0$); b) ^{1}H NMR the precursors in comparison with $MAPbI_3$ all in the MAP/D_2O solvent system; c) ^{1}H NMR spectra of lead propionate (top) and MAP (bottom); d) ^{1}H NMR spectra of MAI in MAP/D_2O (top), MAP in D_2O (middle) and MAI in D_2O (bottom). Chemical shifts reported on a ppm scale related to TMS ($\delta = 0$).

mixture to investigate the chemical interactions in precursor solutions further.

The ^{207}Pb NMR resonance peak of the $MAPbI_3$ perovskite ink is down-field shifted ($\delta^{207}Pb = -198$) compared to the neat $Pb(CH_3CH_2COO)_2$ ($\delta^{207}Pb = -1323$) and $Pb(CH_3COO)_2$ ($\delta^{207}Pb = -1124$) solutions (**Figure** 4a). The deviation of the chemical shifts in the PIL/water-based ink from the neat $Pb(CH_3CH_2COO)_2$ and $Pb(CH_3COO)_2$ lead salts indicates a halide coordination to the $Pb(CH_3COO)_2$ precursor. The down-field shift might be caused by H-bonding to the Pb—I fragments, decreasing the shielding at the Pb centers; however, generally relativistic effects due to the heavy metal Pb might also play a role.

In Figure 4b, ^{1}H NMR spectra of the $MAPbI_3$ (black) precursor ink are shown along with the used precursors CH_3NH_3I (blue) and $Pb(CH_3COO)_2$ (magenta) in MAP/D_2O. The propionate moiety from the ionic liquid ($CH_3CH_2COO^-$) exhibits a triplet from the CH_3 and a quadruplet peak from the CH_2, marked with a rhombus. These peaks are shifted slightly upfield in the $MAPbI_3$ ink compared to the neat precursors in the same solvent system (MAP/D_2O). The methylamine moiety from MAP exhibits a CH_3, singlet peak at $\delta^{1}H = 1.5$ marked with a circle, which is shifted upfield if compared to the neat precursors in the same solvent system. The proton peak at $\delta^{1}H = 2.2$, marked with a black dot, can be assigned to the CH_3 protons of $Pb(CH_3COO)_2$. This peak is slightly shifted compared to the neat lead acetate solution value at $\delta^{1}H = 2.1$. An additional resonance peak at $\delta^{1}H = 0.9$ (marked with a star) might be assigned to a CH_3 group of CH_3NH_3 moiety, whereas the NH_3 group appears at $\delta^{1}H = 4.8$. Please note that this peak also contains the peak of residual water[21] and, due to chemical exchange, leads to a broad peak in all samples. Interestingly, this implies that the protons of methylamine from CH_3NH_3I and the $[CH_3NH_3]^+[CH_3COO]^-$ are not entirely chemically identical. Similarly, in the neat CH_3NH_3I solution, there is also an additional peak at $\delta^{1}H = 2.1$, which can be assigned to a

CH_3 group adjacent to a CO group or a NH_3 group, since the integral of the peak is 3 (Figure S4, Supporting Information) both would be possible. To find out or exclude possible structures, we made further comparisons.

First, comparing the ^{1}H NMR spectrum of a neat lead propionate salt with the ionic liquid (Figure 4c) shows that there is a negligible difference between the characteristic peaks of the propionate moiety (see peaks 4, 5 in $Pb(CH_3CH_2COO)_2$ and 5,6 in MAP spectra). Thus, the upfield shift of these peaks in the ink (Figure 3b) would exclude the full coordination of propionate to the Pb center. As a first conclusion, we can exclude the presence of pure $Pb(CH_3CH_2COO)_2$ species in the $MAPbI_3$ ink.

Second, the addition of MAI to MAP/D_2O significantly changes the solution chemistry, as can be seen in Figure 4d, especially in the shifts of the methylammonium propionate peaks (N—CH_3, CH_2, C—CH_3), as well as in the appearance of the additional peak at $\delta^1H = 2.1$. Furthermore, the H_2O, NH_3 peak is broader, indicating a chemical exchange between protons. Chemically, the difference between both MAI and MAP is the anion, whereas the propionate is in excess compared to iodide since it is used as a co-solvent. Thus, the H-bonding and electrostatic interactions change if iodide is added, leading to these deviations in the chemical shift. As a second conclusion, we claim that the iodide coordination to the Pb centers leads to changes in the H-bonding of the protons in the methylammonium and propionate groups. Thus, we conclude the probable existence of lead iodide structures in the solution rather than lead carboxylates.

Overall, from the ^{1}H NMR analysis, we infer that complexes with mixed ligands are formed where positive (Pb^{2+}, $CH_3NH_3^+$), negative (I^-, CH_3COO^- and $CH_3CH_2COO^-$), and polar solvents interact (H_2O). The ^{207}Pb NMR shifts exclude full coordination of acetate or propionate to the Pb centers. The appearance of additional peaks and the acetate peak in the ^{1}H spectrum of the $MAPbI_3$ ink reveals a mixture of species instead of a single structure. In all ^{207}Pb NMR measurements, a single resonance peak was observed for all measured solutions, indicative of a fast chemical exchange among different lead species on the NMR time scale.[22] Previous reports have identified different iodoplumbate equilibria in perovskite solutions, highlighting the influence of solvent, iodide concentration, and temperature on the chemical shifts.[23–26] Interestingly, our $MAPbI_3$ precursor ink was stable under ambient atmospheric conditions, showing no precipitation or color changes. The shelf stability was also proven by ^{207}Pb and ^{1}H NMR measured over time (Figure S5, Supporting Information).

2.2. Thin Film Fabrication with Green Ink via Slot-Die Coating

For slot-die coating, a number of process and ink parameters determine the quality and homogeneity of coated layers. On the one hand, the distance between the slot-die or shim edge and the substrate surface, *h*, determines the thickness of the wet film (a scheme of the slot-die coater can be found in Figure S6, Supporting Information). In addition, the inks rheological properties like the surface tension, wetting behavior, and viscosity affect the appropriate coating speed during the deposition. As a result, the actual wet film thickness is usually only 60–70% of the theoretical maximum value. Ink properties and process conditions determine the *coating window* of the process, a principle widely used for slot-die coating of adhesives and polymers but underexplored for perovskite ink deposition.[27] It is possible to adjust the desired wet thickness by controlling the web speed according to the rheological properties of the ink. The resulting thin film's thickness, morphology, and microstructure depend on the ink density and composition and the nucleation and crystallization behavior of the halide perovskite semiconductors.[28] This means the deposition depends on the substrate temperature, nitrogen flow rate, and ink solvent system.

Initial trials for the thin film fabrication were performed with water-based ink, which resulted in poor-quality thin films (Figure S7, Supporting Information). The solvent mixture of H_2O/MAP and the solvent mixture plus $MAPbI_3$ precursor (final ink) have a similar dynamic viscosity of 5.8 cp. Using an air knife with a constant N_2 gas flow showed enhanced drying and crystallization compared to the coating without gas quenching. We optimized the ink rheology for the coating process and facilitated solvent removal by adding isopropanol. This solvent engineering was the main improvement factor for the resulting thin films, where an azeotropic H_2O/isopropanol (IPA) (1:7 v/v) mixture was used along with MAP with the composition H_2O/IPA/MAP (5/35/60 v/v%), which led to increased viscosity of 8.4cP for the $MAPbI_3$ ink and decrease in the surface tension (from 67 to 40 mN cm^{-1}) improving the wettability. After further optimizations following the coating window (Figure S14, Supporting Information) of the tuned ink, we could achieve high surface coverage (see Figures S8–S10, Supporting Information for the optimization procedure, including the experimental details and photographs). This improvement is also visible in the thin film morphology (**Figure 5**a,b), where without IPA, there are 2D cracks, and the substrate beneath is visible. With IPA, the thin film is closed although it has 2D islands on top of the absorber layer.

The UV-vis spectra of both $MAPbI_3$ precursor inks in MAP/H_2O and MAP/IPA/H_2O were measured in a cuvette with a path length of 10 µm, enabling the measurement of higher solution concentrations (0.3 M) (Figure 5a). Broad bands are observed for both inks at 222, 277, 335, and 368 nm. A solvent effect is visible upon adding IPA with intensity differences, especially a hyperchromic effect at 368 nm and a slight red shift of its bands. No absorption bands originate from the solvent system in the monitored spectral range (Figure S6, Supporting Information). A comparison of the absorption peak positions with the literature (listed in **Table 1**) reveals some overlap with the absorption band

Table 1. Experimental absorption bands observed in lead halide solutions reported in the literature.[32–35]

	λ [nm] for X=I	Conditions
$Pb(Sol)_6^{2+}$	<250	0.1-1 mM in DMSO
$PbI(Sol)_5^+$	282	0.1-1 mM in DMSO
$PbI_2(Sol)_4$	325	Ten mM-5 mM in DMSO
$[PbI_3(Sol)_3]^-$	367	Ten mM-5 mM in DMSO
$[PbI_4(Sol)_4]^{2-}$	423	10 mM-5 mM in DMSO
$Pb(OH)_2$	227, broad	aq., 9 µM, pH 7.91,
$Pb(OAc)_2$	500	aq., 0.42 M

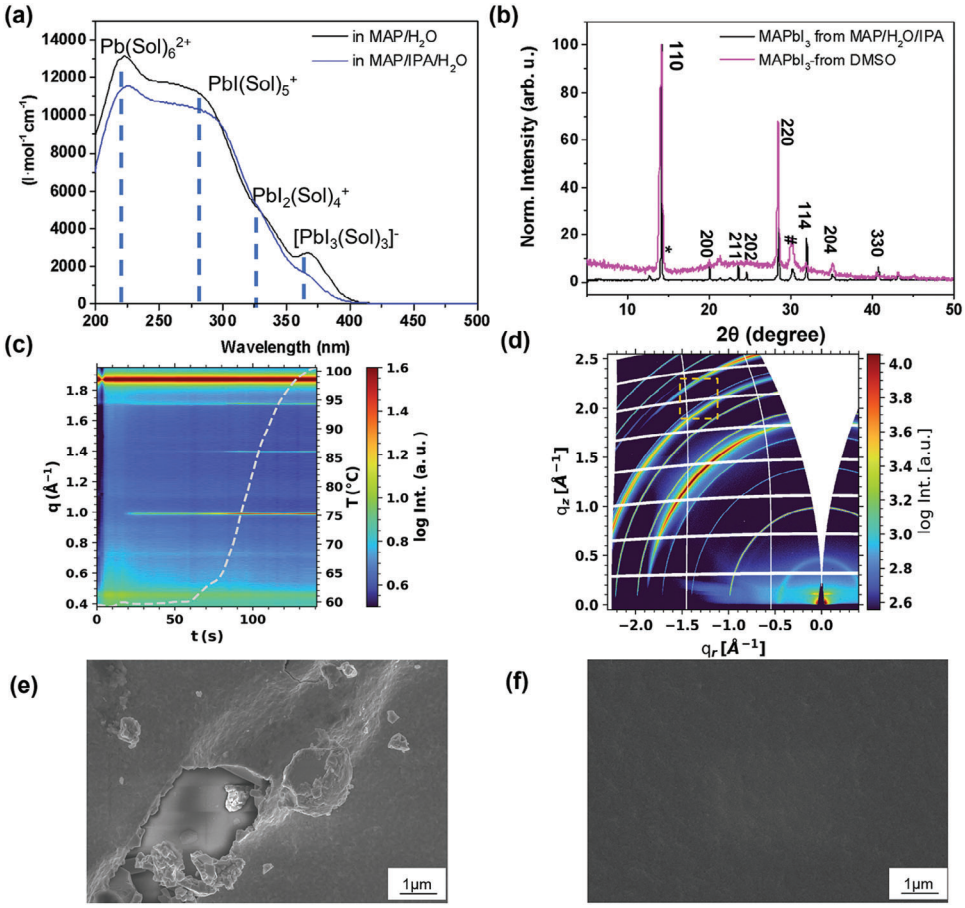

Figure 5. a) UV-vis spectra of 0.3 M $MAPbI_3$ precursor inks in MAP/H_2O (black) and $MAP/IPA/H_2O$ (blue) solvent systems. The inks were measured in a cuvette with a path length of 10 µm, and the spectra were plotted as extinction coefficient versus wavelength; Expected solution species are drawn in the spectra; b) XRD pattern of $MAPbI_3$ thin film from $MAP/H_2O/IPA$ solvent blend (black) in comparison to spin-coated $MAPbI_3$ from DMSO (magenta). PbI_2 is marked with*. The perovskites were coated on pre-cleaned ITO substrates (peak marked with **#**); c) Time evolution of azimuthally integrated radial in-situ GIWAXS patterns ("waterfall plot"). Deposition of green perovskite ink starting at $t = 0$ s, air-knife quenching start at $t = 15$ s, heating start at $t = 75$ s from 60 to 100 °C (indicated in dashed grey with temperature scale on the right axis); d) Reciprocal GIWAXS pattern of the final perovskite thin film after annealing. Scanning electron microscopy images of the slot-die coated perovskite thin layers of the green precursor ink: e) before and f) after the tune of ink and the optimization of the deposition process.

of $[PbI_3(Sol)_3]^-$ being more pronounced in the pure water/MAP-based ink. For p $\leq$ 10.4, it was reported that in aqueous lead solutions, specific absorption bands from 216 to 300 nm were observed, which were assigned to Pb^{2+}, $Pb(OH)^+$, $Pb(OH)_2$, and $Pb(OH)_3^-$. Specifically, pH 7.91 $Pb(OH)_2$ was detected for a 9 µM $Pb(ClO_4)_2$ solution with a maximum extinction coefficient of 2800 M^{-1} cm^{-1}.[29] Also, in PbI_2 solution at low concentration, absorption bands lower than 250 nm were assigned to $[Pb(Sol)_6]^{2+}$ complexes. However, UV-vis absorption spectroscopy is solvent and concentration-sensitive; all conditions for the literature values are noted in the table. Considering this, the $MAPbI_3$ precursor inks, having a pH value of 8, are probably composed of complexes with $Pb(Sol)_6^{2+}$ and $[PbI_3(Sol)_3]^-$ where the solvent ligand might be propionate, acetate, isopropanol or water confirming the results of the ^1H NMR above. Suppose the Lewis basicity of the present ligands is compared. In that case, iodide (donor number DN = 28.9 kcal mol^{-1}[30]) and propionate as anions with free electron pairs and negative charge are highly likely to coordinate to the Pb centers rather than water (DN = 18 kcal mol^{-1})[31] or isopropanol. Again, the measurement confirms that the solution is composed of various species.

The XRD pattern of the $MAPbI_3$ thin film from the $MAP/IPA/H_2O$ (Figure 5b, black) shows the formation of a crystalline perovskite with prominent tetragonal peaks at 2θ ≈14° (110), 28° (220), and 43° (330) comparable to a thin film obtained from a spin-coated DMSO solution (magenta). However, the XRD pattern also contains other crystal planes coming from (200), (211), (202), (114), and (204), hinting at a typical disordered crystallite orientation in the polycrystalline perovskite thin film.

To monitor the liquid-to-solid transition during the thin film formation process, in-situ grazing-incidence wide-angle X-ray scattering (GIWAXS) measurements[36] were conducted during the doctor-blading of the $MAPbI_3$ $MAP/IPA/H_2O$ ink, N_2 quenching, and annealing. As shown in Figure 5c, the tetragonal (110) $MAPbI_3$ reflex at ≈1 $Å^{-1}$ occurs after a few seconds of N_2 quenching and drying of the ink. Interestingly, the reflex does not show significant texture but rather an isotropic crystallite distribution. No tetragonal (200) intensity or reflexes of higher

Miller indices can be unambiguously detected, likely due to the relatively weak overall perovskite intensity. Upon temperature increase, the (110) and (200) $MAPbI_3$ reflexes become more pronounced, and perovskite reflexes of higher order can be detected. Here, we note that the crystallization from solution to $MAPbI_3$ usually occurs via crystalline complex phases connected to lead plumbates coordinated with strongly coordinating solvents such as DMSO.[37] In this present case, only a very weak transient reflex can be seen during quenching that could be possibly attributed to a Pb_2I_6-structured complex (Figure S7, Supporting Information), which, according to literature, is found at around $2\theta = 7°$, in particular in inks with DMF and DMSO.[38]

This ring has only a fragile intensity and co-occurs with the (110) $MAPbI_3$ reflex, indicating that the main route of the perovskite conversion does not occur via any known intermediate phase and no other crystalline intermediate phase wasobservable in GIWAXS. Interestingly, no evidence of a $MAPbI_3$ hydrate phase with water, hypothetically giving rise to a peak at $2\theta = 8.7°$,[39[could be observed during the entire in-situ experiment either. The present ligands in the ink do not bind strongly to the lead centers, as inferred from NMR, IR, and UV/vis, where no pronounced coordination was found.

The final perovskite film (Figure 5d) shows a relatively isotropic crystallite distribution without pronounced texture. The system indicates substantially different properties than $MAPbI_3$ films derived from classical solvent systems in DMF and DMSO.[37,40] Furthermore, no lead iodide species could be detected in GIWAXS, indicating that no PbI_2 is formed during the chemical reaction. This is important to emphasize since the XRD data in Figure 5d shows a small PbI_2 peak at $2\theta = 12°$ for the MAP/IPA/H_2O-derived film, while this feature is not apparent in the XRD of the film derived from pure DMSO or covered by noise. Therefore, we repeated the XRD measurement on freshly made thin films, annealed and non-annealed, and measured immediately, showing no appearance of PbI2; furthermore, the perovskite thin films with IPA addition showed a slightly better crystallinity (Figure S13, Supporting Information). Thus, we can confirm that this PbI_2 observed in XRD is not necessarily a product of film formation from the green ink but a result of sample exposure to ambient conditions.

$MAPbI_3$-based solar cells were fabricated to test the newly formulated ink's applicability. For this purpose, a p-i-n architecture was used based on the ITO/2PACz/$MAPbI_3$/C_{60}/BCP/Cu stack where 2PACz is 2-(9H-carbazol-9-yl) ethyl] phosphonic acid used as the hole transporting material and C_{60} and bathocuproine (BCP) are the electron transporting and buffer layers. The optimized H_2O/IPA/MAP solvent system and use of N_2 gas quenching during the thin film deposition process at 60–70 °C substrate temperatures with coating speeds ≈10–15 cm min^{-1} and an ink flux of 15–30 µL min^{-1} (coating windows showed in Figure S8, Supporting Information) yielded a high surface coverage and uniform thin films (Figure 5e,f). The top view SEM images of the perovskite thin films reveal that this solvent system induced a pattern during the crystallization process. Having a good film before adding the IPA to the ink formulation is impossible. The wettability of the precursor is very bad on the SAM layer, and the pinholes are primarily due to the poor coverage of the perovskite. Adding the IPA improves the wettability, and after the optimization process, the pinholes disappear entirely due to the natural convection evaporation of the solvent. This highlights the importance of controlling both the coating parameters (through the coating window shown in Figure S14, Supporting Information) and the evaporation of the solvent system, a process that starts with the addition of the isopropanol in the ink to tune the evaporation rate of the solvents.

The cross-section scanning electron micrograph shows intact interfaces without pinholes (**Figure 6a**). The perovskite thin film was deposited via slot-die coating with the above-mentioned optimized parameter, while 2PACz was spin-coated, and the materials C_{60}, BCP, and Cu were evaporated. The champion solar cell achieved a PCE of 10.3% with 17.2 mA cm^{-2} short current density (J_{SC}), 0.93 V for open circuit voltage (V_{OC}), and a fill factor (FF) of 0.65 for the forward scan and 9.35% PCE, 17.2 mA cm^{-2}, 0.86 V and 0.63 for FF for the reverse scan, showing a small hysteresis. The external quantum efficiency (EQE) measurement could extract a J_{SC} of 16.59 mA cm^{-2}, showing that the JV curve is reasonably accurate (Figure 6c).

Thus, our solar cell performance is comparable to the literature values (Figure 1) but using a one-step and scalable solution method instead of sequential deposition. Although the spread of solar cell performances is not small, as can be seen from the box plots in Figure S15 (Supporting Information), several other factors, such as the sensitivity of the 2PACz toward IPA or water, as well as possibly remaining water degrading the perovskite thin film can lead to reduced performances – influence factors that need further investigation and will be the focus in future studies.

To track the stability, one batch of 15 solar cells was manufactured; the best five devices were measured on the maximum power point (MPP) for 1 h during 20 days, and the results are shown in **Figure 7**. After three days, many of the best devices dropped performance by ≈2%. Still, they remained pretty stable until day ten, after most devices lost around 50% of their efficiency.

2.3. Life Cycle Assessment of the PIL-Based Ink

To evaluate the ink's relative environmental impact, a comprehensive gate-to-gate comparison between a standard $MAPbI_3$ DMF/DMSO ink was prepared according to Ahn et al.,[41] and the PIL-based $MAPbI_3$/MAP/IPA/H_2O ink was conducted using 1 mL of each. The energy consumption during the deposition process was assumed to be uniform for both variants. Our assessment focuses on synthesizing each ink's chemical precursors and processes while disregarding waste, recycling, and device efficiency factors. Details on the life cycle impact assessment (LCIA) analysis performed are provided in Figures S15 and S16 (Supporting Information). A standardized LCIA comparison done by openLCA compares the sample based on two main categories: environmental and human health impact; of these two main categories, there are 25 subcategories, as seen in **Figure 8**.

Within the data, comparisons for the impact categories related to human health include nine subcategories (**Table 2**). Human toxicity impacts are commonly reported in comparative Toxic Units for Humans (CTUh), representing the estimated mortality increase for the total human population per unit mass of chemical emitted. Additional impact categories considered are particulate matter formation (1), photochemical oxidant formation (2),

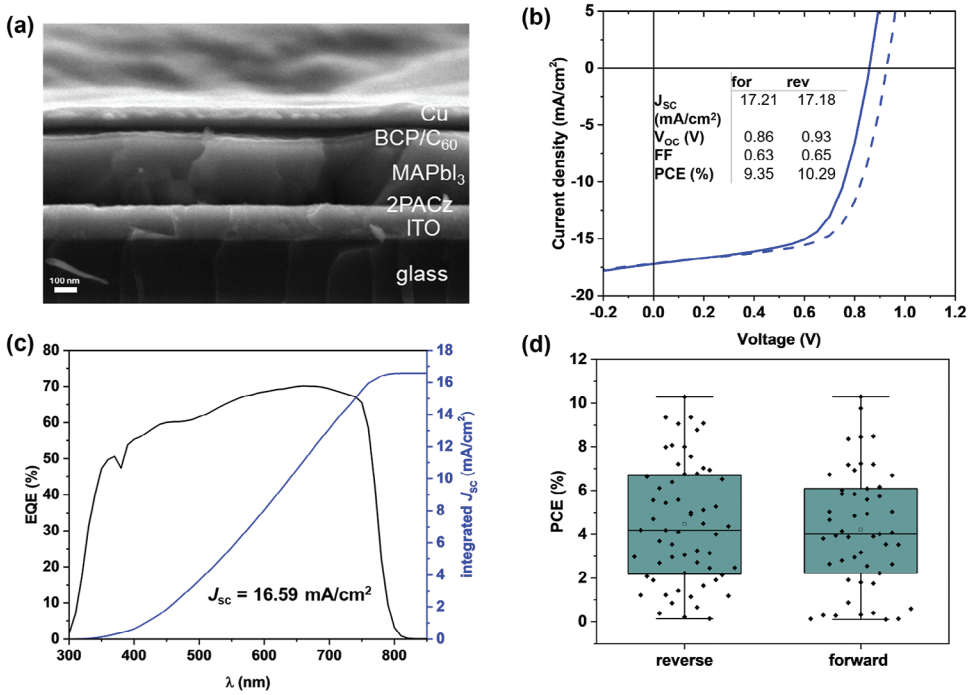

Figure 6. Champion solar cell device fabricated from a slot-die coating of $MAPbI_3$ MAP/IPA/H_2O ink; a) Cross-section SEM of a device with the p-i-n structure showing the interfaces, note the organic HTL and ETL are too thin to be visible; b) JV curves in forward (solid line) and reversed (dashed line) scan under 1 Sun illumination and light soaking of 60 s; c) EQE of the best solar cell. Measured from 300 nm to 850 nm with a step size of 10 nm; d) Boxplots of PCE for 53 solar cells (1 device has 6 pixels with an area of 0.16 cm^2 each) in reverse and forward scan under 1 Sun illumination and a light soaking time of 60 s.

and ionizing radiation (7). These are measured in disease incidence, equivalent kilograms of non-methane volatile organic compounds (NMVOCs), and the decline in human health due to air quality deterioration, respectively. These impacts were calculated using midpoint methods, focusing solely on the chemical-to-ink system, thus constituting a gate-to-gate study.

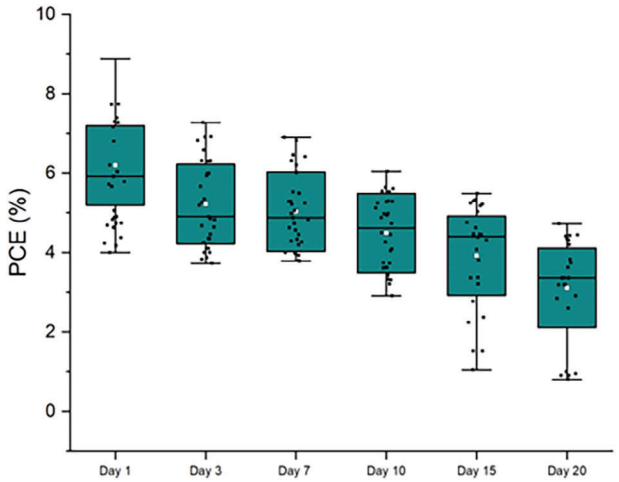

Figure 7. Boxplots of PCE evolution during 20 days for five solar cells (1 device has 6 pixels with an area of 0.16 cm^2 each) in reverse and forward scan under 1 Sun illumination for 1 h.

Table 2 shows a reduction in all areas impacting human health when using the greener ink, resulting in a decreased negative health impact. Specifically, human toxicity carcinogenic (11) decreased by ≈20%, and human toxicity non-carcinogenic (16) decreased by about 80%. Ionizing radiation (7) decreased by 4%, and photochemical oxidant formation (2) decreased by 16% between the two methods. These results suggest that using a greener solvent may reduce the potential for adverse human health effects in the future.

Overall, the $MAPbI_3$ ink created using green solvents showed improvements in all measured areas except ozone depletion (25) and non-renewable energy consumption (8). This indicates that the synthesis process for the materials used in the green ink solvent has higher ozone depletion potentials and requires more energy, likely sourced from non-renewable resources. However, the relative increases are modest—only 10% for non-renewable energy resources and 20% for ozone depletion. Moreover, the slight negative impact on energy efficiency during ink synthesis is likely offset by the energy-saving potential of switching to a green solvent-based $MAPbI_3$ ink, as this approach eliminates the need for gloveboxes and allows for processing at lower temperatures compared to the standard ink. Eventually, suggesting significant environmental and practical advantages, including reduced operational costs and enhanced safety. The lower processing temperatures could also lead to broader applicability and easier scalability in industrial settings.

This study presents a promising pathway toward more sustainable perovskite solar cell production by developing a green, water-based $MAPbI_3$ ink with methylammonium propionate as a

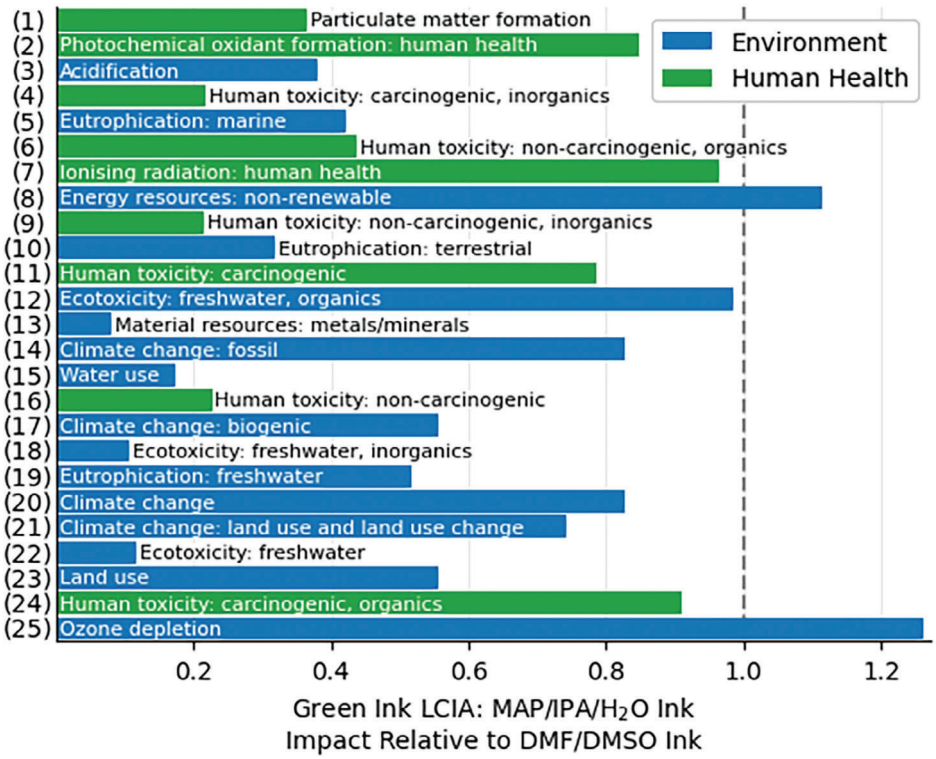

Figure 8. Results of the comparative LCIA analysis between the standard $MAPbI_3$ DMF/DMSO ink and $MAPbI_3$ MAP/IPA/H_2O ink. For each indicator, the result of the standard ink is set to 1, and the results of the green ink are displayed to it. See Table S2 (Supporting Information) for exact values and indicators.

protic ionic liquid (PIL) ink additive. Using isopropanol to enhance processability, we successfully utilized a one-step slot-die coating technique to fabricate high-quality perovskite thin films, demonstrating scalable potential. In-situ GIWAXS measurements revealed a direct transition to the perovskite phase with negligible PbI_2 formation during crystallization, even under ambient conditions without controlled humidity. This highlights the adaptability of our ink formulation to practical, uncontrolled environments. However, the appearance of PbI_2 in the steady-state XRD of stored films points to the need for further strategies to improve long-term stability.

This approach represents a balanced strategy for advancing perovskite solar cells, combining effective device performance with a reduced environmental footprint, and offering tangible advantages for industrial applications. As a next step, further work will focus on scaling approaches to develop larger-area devices, including fabricating perovskite minimodules to demonstrate practical viability on an industrial scale. This will involve optimizing coating techniques, such as refining slot-die coating parameters, to maintain uniformity and performance across larger surfaces. By addressing these challenges, this green solvent-based method can potentially support the development of efficient, stable, and environmentally friendly perovskite solar modules for real-world applications.

Table 2. Comparison of the LCIA calculations of the green $MAPbI_3$ ink in MAP/IPA/H_2O and the standard $MAPbI_3$ in DMF/DMSO. The percentages show a decrease compared to the standard ink.

Number	Impact category	Predicted difference between the green and standard ink [%] (Green/Standard)*100%
1	Particulate matter formation	60%
2	Photochemical oxidant formation	15%
4	Human toxicity; carcinogenic, inorganic	80%
6	Human toxicity; non-carcinogenic, organic	55%
7	Ionizing radiation: human health	4%
9	Human toxicity: non-carcinogenic, inorganics	80%
11	Human toxicity: carcinogenic	20%
16	Human toxicity: non-carcinogenic	75%
24	Human toxicity: carcinogenic, organic	9%

3. Conclusion

In this study, we successfully minimized the toxic content of perovskite precursor inks through solvent engineering based on water and isopropanol, using the protic ionic liquid (PIL) methyl ammonium propionate (MAP) as an ink additive. MAP enabled the dissolution of lead salts in non-toxic solvents, developing a long-term stable perovskite precursor ink containing 5% water. Dynamic solution chemistry studies, including NMR, UV-vis,

and IR, suggested the presence of iodoplumbates in dynamic equilibrium with partial carboxylate coordination. At the same time, GIWAXS revealed non-intermediate-driven crystallization, resulting in polycrystalline tetragonal $MAPbI_3$.

Also, the precursor's rheology makes it possible to use the ink for the processing of the halide perovskite using scalable slot-die coating as the deposition method. The solvents' non-toxic nature and the inclusion of IPA in an azeotropic ratio with the water allow the ink to be employed at ambient conditions to fabricate p-i-n solar cells with a glass/ITO/2PACz/$MAPbI_3$/C60/BCP/Cu stack, achieving a champion PCE of up to 10%. This is the first report on a one-step water-based ink with these characteristics.

Moreover, our life cycle impact assessment (LCIA) analysis demonstrated that the new ink formulation is significantly more environmentally friendly than the conventional DMF/DMSO-based ink, showing reduced human toxicity.

This work introduces a greener alternative to traditional perovskite inks and opens new avenues for the scalable and environmentally sustainable production of perovskite solar cells under ambient conditions. The successful integration of water-based ink in a scalable deposition method like slot-die coating could significantly impact the perovskite solar cell research field, paving the way for more sustainable and cost-effective manufacturing processes.

4. Experimental Section

Materials: Bathocuproine (BCP) and C_{60} were purchased from Ossilla at a grade exceeding 99.5%. [2-(9*H*-carbazol-9-yl) ethyl] phosphonic acid (2PACz) was purchased from TCI Chemicals at a purity level exceeding 98%. Copper pellets were purchased from Evochem at a purity level of 99.99%. Deuterium oxide (D_2O), sourced from Deutero, was utilized at a grade of 99.9% with an additional tolerance of +0.03% TMS. Ethanol, acquired from Fischer Scientific, was of absolute grade to ensure purity throughout the experiments. Hellmanex III, procured from Hellma Analytics, was utilized as a 2% aqueous solution. Isopropanol, acquired from Acros Organics, was used in its technical grade form. Lead (II) acetate was purchased from TCI chemicals as a perovskite precursor. Methylamine, obtained from TCI, was used at 40 wt.% in methanol (MeOH). Methylammonium iodide (MAI) was purchased from Dyenamo. Propionic acid, acquired from Sigma Aldrich, was utilized at a purity level exceeding 99.5%. Commercial patterned indium tin oxide-coated glass substrates from *Automatic Research* with a resistivity of 15 Ω cm^{-2} were used for solar cell fabrication.

Synthesis of Methylammonium Propionate (MAP): 34 mL (25.84 g, 0.332 mol, 1 eq.) of methylamine solution (40 wt.% in MeOH) was cooled in an ice bath. 25 mL (24.75 g, 0.332 mol, 1 eq.) of propionic acid was slowly added over 15 min, and the mixture was stirred for 1 h. The methanol was removed under reduced pressure with a rotary evaporator, and the product was received as a clear and viscous liquid.

Preparation of Water-Based Perovskite Precursor Ink ($MAPbI_3$ in MAP/H_2O): 0.5204 g (1.6 mmol, 1 eq.) lead acetate ($Pb(OAc)_2$) and 4.8 mmol (3 eq.) of methylammonium iodide (MAI) were dissolved in 2.0 mL water and 3.0 mL methylammonium propionate (MAP). The mixture was stirred at 50 °C until a clear solution was obtained and stored under ambient conditions.

Preparation of Water-and IPA-Based Perovskite Precursor Ink ($MAPbI_3$ in $MAP/IPA/H_2O$): 0.5204 g (1.6 mmol, 1 eq.) lead acetate ($Pb(OAc)_2$) and 4.8 mmol (3 eq.) of methylammonium iodide (MAI) were dissolved in 1.75 mL IPA, 0.25 mL water and 3 g (3.0 mL) methylammonium propionate (MAP). The mixture was stirred at 50 °C temperature until a clear solution was obtained and stored under ambient conditions.

Solar Cell Fabrication: Patterned ITO substrates (25 × 25 mm) were cleaned using 2% *Hellmanex III* solution, deionized water, acetone, and isopropanol in an ultrasonic bath for 10–15 min each. Before further use, they were kept in a UV-ozone chamber for at least 15 min. For the hole transporting layer, a solution of 3 mmol 2PACz in ethanol was spin-coated on the cleaned ITO substrates (35 s, 3000 rpm, 600 rpm s^{-1}) and annealed at 100 °C for 10 min. After that, these substrates were slot-die coated (sheet coater from FOM Technologies) with the $MAPbI_3$ in $MAP/IPA/H_2O$ ink using a N_2 knife (10° angle and 1 mm gap to the surface, pressure of 25 psi). The distance of the slot-die head to the substrates was 100 µm, and the flux of the ink pumped through the slot-die head was 30 µL min^{-1}. The substrate coating speed was 15 cm min^{-1}, and the temperature was 60 °C. The substrates were transferred on a hot plate at 100 °C for 15–20 min in an ambient atmosphere for final annealing. Then, they were assigned to a nitrogen-filled glovebox to evaporate the electron transport materials (23 nm C_{60} and 8 nm BCP) and 100 nm copper electrode.

X-Ray Diffraction: The XRD measurements were done in a *Bruker D8* diffractometer with Cu Kα (λ = 1.5406 Å) operated at 40 kV and 40 mA in Bragg-Brentano geometry.

FT-IR: A *Spectrum 400 FT-IR/FT-FIR* Spectrometer from *PerkinElmer* was used for the FT-IR measurements of perovskite precursor inks. The measurements were conducted under ambient atmospheric conditions, and a 2 µL volume was used for each sample.

Mass Spectrometry: The mass spectrometry experiment was conducted with a quadrupole QMS 220 M3 mass spectrometer from Pfeiffer. Electron ionization at 70 V was applied using iridium filaments coated with yttrium. Detection was performed with a secondary electron multiplier set to 940 V. The mass filter time was adjusted to 100 ms per amu. The wet film was initially used as an additive to freeze in nitrogen and then transferred into the spectrometer chamber. It was gradually heated, allowing released molecules to be detected over time.

Nuclear Magnetic Resonance (NMR) Spectroscopy: NMR spectra were acquired using a Bruker Avance II 300 spectrometer, operating at 300.1 MHz for proton (^{1}H) and 62.9 MHz for lead (^{207}Pb), equipped with a 5 mm BBO ATM probe. The ^{207}Pb resonance was detected using a proton broadband decoupled ^{207}Pb{H} experiment. Chemical shifts for ^{1}H are reported in parts per million (ppm) relative to tetramethylsilane (TMS, δ = 0), internally referenced to the residual proton signals of the lock solvent. ^{207}Pb chemical shifts were externally referenced to a 1.0 M $Pb(NO_3)_2$ solution in D_2O (δ = −2986.3 ppm) and are reported relative to $Pb(CH_3)_4$ in toluene (δ = 0).

Surface Tension: The surface tension of the inks on air was measured in a drop-shape analyzer from *Krüss using a 1 mL syringe and* a 0.8 mm diameter needle.

UV-Vis Absorption Spectroscopy: To measure the UV-vis absorption spectra, *Cary 5000 UV-Vis-NIR* from *Agilent* was used utilizing cuvettes from *Hellma Analytics* (*type 106-QS*) with a path length of 10 µm.

Grazing-Incidence Wide-Angle X-Ray Scattering (GIWAXS): GIWAXS data were taken with a Pilatus 3 M (Dectris) at an energy of 10 keV at the I07 beamline at the Diamond Light Source, UK. The green ink was coated with a mobile blade-coating setup described elsewhere.[46] In-situ data was collected at an incident angle of 1°, and a repeated horizontal scan with attenuation was performed to avoid beam damage of the sensitive liquid phase, with 0.1 s exposure time per frame and ≈2 s time resolution. Static data was collected by performing a horizontal scan and summing up the counts in the data analysis. Scattering data processing was done with the Python tool INSIGHT, including transformation to q-space, geometric calculations, intensity corrections for path attenuation, detector absorption, photon polarization, and solid angle.[47] The correction of the sample-to-detector distance was done by calibrating the substrate's (110) FTO reflex to 1.87 $Å^{-1}$, neglecting lattice expansion within the temperature range used (60 °C–100 °C).

Solar Cell Testing: The current-voltage (JV) curves were measured with a Keithley 2450 Source Meter on a calibrated AM1.5 spectrum of a class AAA solar simulator from Sciencetech with an illumination area of 50 × 50 mm, providing a power density of 100 mW cm^2. The −0.2 to 1.2 V range was screened for the forward scan, and the backward scan was screened for 1.2 to −0.2 V with a scan speed of 0.5 V s^{-1}). The illuminated areas

of the cells were 0.16 cm^2 using patterned ITO substrates. The EQE was measured using an Enlitech setup with a step size of 10 nm.

Life Cycle Impact Assessment: Human health impacts were assessed by considering specific impact categories calculated using OpenLCA 2.1. software (https://openlca.org) and the *ecoinvent* database. The standard unit for reporting human toxicity impacts is in CTUh, which is the estimated increase in mortality for the total human population per unit mass of chemical emitted. Other impact categories considered are particulate matter formation, photochemical oxidant formation, and ionizing radiation, measured in disease incidence, equivalent kilograms of non-methane volatile organic compounds, and decline in human health due to deterioration of air quality, respectively. These impacts were calculated with endpoint methods that only looked at the impact of a system earlier in its life cycle, which was considered a gate-to-gate study.

Supporting Information

Supporting Information is available from the Wiley Online Library or from the author.

Acknowledgements

The authors would like to thank Diamond Light Source for beamtime (proposal SI36427) and the staff of beamline I07 for assistance. Furthermore, the authors kindly acknowledge the support of the NMR facility at the University of Cologne for providing access to the NMR spectrometers. F.Ü, E.U., and L.K.R. acknowledge funding from the HGF-funded project SolarTAP and the DFG-funded project GLIMPSE. A.F. acknowledges funding from Alianza SÉNECA and the VIPER Lab Project for the financing. S.O. acknowledges funding by the Horizon Europe project HEPAFLEX under grant agreement No. 101122345. F.Ü. and S.M. acknowledge funding from the DFG-funded project ASTRAL.

Conflict of Interest

The PILs utilised in this work are commercially available from the company Solaveni GmbH, led by co-author Senol Öz.

Author Contributions

F.Ü. and A.F contributed equally to this work. F.Ü. and A.F. contributed to the research design and implementation and the analysis of the results. F.Ü. took the lead in writing the manuscript with the support from A.F., K.D.-O., and L.K.R. L.K.R. and F.Y. conducted the in-situ GIWAX analysis. M.G. conducted the MS analysis. S.O. and F.M. co-supervised the project and discussed results, and S.M. and E.U. led the project, enabling administrative and funding support. All authors contributed to the final version of the manuscript.

Data Availability Statement

The data for this paper was stored in a NOMAD Oasis at HZB, piloting a FAIRer (findable, accessible, interoperable, and reusable) way of data sharing. The data schema utilizes the thin-film solar cell ontology (TFSCO). The relevant data can be seen by clicking here. Clicking entries will jump you to the respective solar cell and its synthesis information. This overview (click here) will show the JV data, and clicking it will jump you to the respective JV curves. The DOI for the dataset on the NOMAD Oasis is https://doi.org/10.17172/NOMAD/2024.09.25-1.

Keywords

non-toxic solvents, one-step processing, protic ionic liquids, slot-die coating, water-based perovskite ink

Received: August 14, 2024
Revised: November 30, 2024
Published online:

[1] L. Schmidt-Mende, V. Dyakonov, S. Olthof, F. Ünlü, K. M. T. Lê, S. Mathur, A. D. Karabanov, D. C. Lupascu, L. M. Herz, A. Hinderhofer, F. Schreiber, A. Chernikov, D. A. Egger, O. Shargaieva, C. Cocchi, E. Unger, M. Saliba, M. M. Byranvand, M. Kroll, F. Nehm, K. Leo, A. Redinger, J. Höcker, T. Kirchartz, J. Warby, E. Gutierrez-Partida, D. Neher, M. Stolterfoht, U. Würfel, M. Unmüssig, et al., *APL Mater.* **2021**, *9*, 109202.
[2] J. C. Hamill, J. Schwartz, Y. L. Loo, *ACS Energy Lett.* **2018**, *3*, 92.
[3] D. T. Moore, H. Sai, K. W. Tan, D.-M. Smilgies, W. Zhang, H. J. Snaith, U. Wiesner, L. A. Estroff, *J. Am. Chem. Soc.* **2015**, *137*, 2350.
[4] A. Sharenko, C. Mackeen, L. Jewell, F. Bridges, M. F. Toney, *Chem. Mater.* **2017**, *29*, 1315.
[5] T. J. Jacobsson, A. Hultqvist, A. García-Fernández, A. Anand, A. Al-Ashouri, A. Hagfeldt, A. Crovetto, A. Abate, A. G. Ricciardulli, A. Vijayan, A. Kulkarni, A. Y. Anderson, B. P. Darwich, B. Yang, B. L. Coles, C. A. R. Perini, C. Rehermann, D. Ramirez, D. Fairen-Jimenez, D. Di Girolamo, D. Jia, E. Avila, E. J. Juarez-Perez, F. Baumann, F. Mathies, G. S. A. González, G. Boschloo, G. Nasti, G. Paramasivam, G. Martínez-Denegri, et al., *Nat. Energy* **2022**, *7*, 107.
[6] M. T. Hoang, F. Ünlü, W. Martens, J. Bell, S. Mathur, H. Wang, *Green Chem.* **2021**, *23*, 5302.
[7] Y. Miao, M. Ren, Y. Chen, H. Wang, H. Chen, X. Liu, T. Wang, Y. Zhao, *Nat. Sustain.* **2023**, *6*, 1465.
[8] D. Liu, C. J. Traverse, P. Chen, M. Elinski, C. Yang, L. Wang, M. Young, R. R. Lunt, *Adv. Sci.* **2018**, *5*, 1700484.
[9] C. Du, S. Wang, X. Miao, W. Sun, Y. Zhu, C. Wang, R. Ma, *Beilstein J. Nanotechnol.* **2019**, *10*, 2374.
[10] X. Cao, G. Zhang, L. Jiang, Y. Cai, Y. Gao, W. Yang, X. He, Q. Zeng, G. Xing, Y. Jia, J. Wei, *ACS Appl. Mater. Interfaces* **2020**, *12*, 5925.
[11] X. Cao, G. Zhang, Y. Cai, L. Jiang, X. He, Q. Zeng, J. Wei, Y. Jia, G. Xing, W. Huang, *Sol. RRL* **2020**, *4*, 2000008.
[12] N. Ali, C. Liang, C. Ji, H. Zhang, M. Sun, D. Li, F. You, Z. He, *Org. Electron.* **2020**, *84*, 105805.
[13] J.-Y. Seo, T. Matsui, J. Luo, J.-P. Correa-Baena, F. Giordano, M. Saliba, K. Schenk, A. Ummadisingu, K. Domanski, M. Hadadian, A. Hagfeldt, S. M. Zakeeruddin, U. Steiner, M. Grätzel, A. Abate, *Adv. Energy Mater.* **2016**, *6*, 1600767.
[14] D. Liu, Z. Shao, J. Gui, M. Chen, M. Liu, G. Cui, S. Pang, Y. Zhou, *Chem. Commun.* **2019**, *55*, 11059.
[15] W. Cai, Z. Zang, L. Ding, *J. Semicond.* **2021**, *42*, 080201.
[16] S. Öz, J. Burschka, E. Jung, R. Bhattacharjee, T. Fischer, A. Mettenbörger, H. Wang, S. Mathur, *Nano Energy* **2018**, *51*, 632.
[17] K. Lê, F. von Toperczer, F. Ünlü, G. Paramasivam, F. Mathies, E. Nandayapa, E. J. W. List-Kratochvil, T. Fischer, K. Lindfors, S. Mathur, *Adv. Eng. Mater.* **2023**, *25*, 2201651.
[18] Y. Tu, J. Ye, G. Yang, Y. Zang, L. Zhang, Y. Wang, G. Li, L. Chu, W. Yan, *J. Alloys Compd.* **2023**, *942*, 169104.
[19] E. Rezaee, D. I. Kutsarov, J. Zhang, G. Koutsourakis, B. Li, F. A. Castro, S. Ravi, P. Silva, *Small Methods* **2024**, *8*, 2300564.
[20] IFA GESTIS-Stoffdatenbank, https://gestis.dguv.de/ (accessed: February 2022).
[21] G. R. Fulmer, A. J. M. Miller, N. H. Sherden, H. E. Gottlieb, A. Nudelman, B. M. Stoltz, J. E. Bercaw, K. I. Goldberg, *Organometallics* **2010**, *29*, 2176.
[22] R. S. Macomber, *J. Chem. Educ.* **1992**, *69*, 375.
[23] S. A. Fateev, A. A. Petrov, V. N. Khrustalev, P. V. Dorovatovskii, Y. V. Zubavichus, E. A. Goodilin, A. B. Tarasov, *Chem. Mater.* **2018**, *30*, 5237.

[24] K. G. Stamplecoskie, J. S. Manser, P. V. Kamat, *Energy Environ. Sci.* **2015**, *8*, 208.
[25] B. A. Sorenson, L. U. Yoon, E. Holmgren, J. J. Choi, P. Clancy, *J. Mater. Chem. A* **2021**, *9*, 3668.
[26] P. K. Nayak, D. T. Moore, B. Wenger, S. Nayak, A. A. Haghighirad, A. Fineberg, N. K. Noel, O. G. Reid, G. Rumbles, P. Kukura, K. A. Vincent, H. J. Snaith, *Nat. Commun.* **2016**, *7*, 13303.
[27] O. J. Romero, L. E. Scriven, M. S. Carvalho, *J. Nonnewton. Fluid Mech.* **2006**, *138*, 63.
[28] A. Berni, M. Mennig, H. Schmidt, in *Sol-Gel Technologies for Glass Producers and Users*, Vol. *21* (Eds: M. A. Aegerter, M. Mennig), Springer, New York US **2004**, 89.
[29] W. Nimal Perera, G. Hefter, P. M. Sipos, *Inorg. Chem.* **2001**, *40*, 3974.
[30] W. Linert, R. F. Jameson, A. Taha, *J. Chem. Soc. Dalt. Trans.* **1993**, https://pubs.rsc.org/en/content/articlelanding/1993/dt/dt9930003181.
[31] V. Gutmann, *The Donor-Acceptor Approach to Molecular Interactions*, Springer, Berlin **1978**.
[32] O. Shargaieva, L. Kuske, J. Rappich, E. Unger, N. H. Nickel, *ChemPhysChem* **2020**, *21*, 2327.
[33] S. J. Yoon, K. G. Stamplecoskie, P. V. Kamat, *J. Phys. Chem. Lett.* **2016**, *7*, 1368.
[34] E. Radicchi, E. Mosconi, F. Elisei, F. Nunzi, F. De Angelis, *ACS Appl. Energy Mater.* **2019**, *2*, 3400.
[35] K. Oldenburg, A. Vogler, *Zeitschrift fur Naturforsch. – Sect. B J. Chem. Sci.* **1993**, *48*, 1519.
[36] J. A. Steele, E. Solano, D. Hardy, D. Dayton, D. Ladd, K. White, P. Chen, J. Hou, H. Huang, R. A. Saha, L. Wang, F. Gao, J. Hofkens, M. B. J. Roeffaers, D. Chernyshov, M. F. Toney, *Adv. Energy Mater.* **2023**, *13*, 2300760.
[37] M. A. Reus, L. K. Reb, A. F. Weinzierl, C. L. Weindl, R. Guo, T. Xiao, M. Schwartzkopf, A. Chumakov, S. V. Roth, P. Müller-Buschbaum, *Adv. Opt. Mater.* **2022**, *10*, 2102722.
[38] A. A. Petrov, I. P. Sokolova, N. A. Belich, G. S. Peters, P. V. Dorovatovskii, Y. V. Zubavichus, V. N. Khrustalev, A. V. Petrov, M. Grätzel, E. A. Goodilin, A. B. Tarasov, *J. Phys. Chem. C* **2017**, *121*, 20739.
[39] F. Hao, C. C. Stoumpos, Z. Liu, R. P. H. Chang, M. G. Kanatzidis, *J. Am. Chem. Soc.* **2014**, *136*, 16411.
[40] L. Oesinghaus, J. Schlipf, N. Giesbrecht, L. Song, Y. Hu, T. Bein, P. Docampo, P. Müller-Buschbaum, *Adv. Mater. Interfaces* **2016**, *3*, 1600403.
[41] N. Ahn, D.-Y. Son, I.-H. Jang, S. M. Kang, M. Choi, N.-G. Park, *J. Am. Chem. Soc.* **2015**, *137*, 8696.
[42] M. T. Hoang, Y. Yang, N. D. Pham, H. Wang, *J. Phys. Chem. Lett.* **2024**, *15*, 6880.
[43] Y. Cui, S. Wang, L. Ding, F. Hao, *Adv. Energy Sustain. Res.* **2021**, *2*, 2.
[44] L. Zhang, H. Li, K. Zhang, W. Li, C. Zuo, G. O. Odunmbaku, J. Chen, C. Chen, L. Zhang, R. Li, Y. Gao, B. Xu, J. Chen, Y. Liu, Y. Wang, Y. Song, J. Tang, F. Gao, Q. Zhao, Y. Peng, M. Liu, L. Tao, Y. Li, Z. Fang, M. Cheng, K. Sun, D. Zhao, Y. Zhao, S. Yang, C. Yi, et al., *iEnergy* **2023**, *2*, 172.
[45] H. Chen, C. Liu, J. Xu, A. Maxwell, W. Zhou, Y. Yang, Q. Zhou, A. S. R. Bati, H. Wan, Z. Wang, L. Zeng, J. Wang, P. Serles, Y. Liu, S. Teale, Y. Liu, M. I. Saidaminov, M. Li, N. Rolston, S. Hoogland, T. Filleter, M. G. Kanatzidis, B. Chen, Z. Ning, E. H. Sargent, *Science* **2024**, *384*, 189.
[46] D. T. W. Toolan, M. P. Weir, S. Wang, S. A. Dowland, Z. Zhang, J. Xiao, J. Rawle, N. Greenham, R. H. Friend, A. Rao, R. A. L. Jones, A. J. Ryan, *Nanoscale Horiz.* **2023**, *8*, 1090.
[47] M. A. Reus, L. K. Reb, D. P. Kosbahn, S. V. Roth, P. Müller-Buschbaum, *J. Appl. Crystallogr.* **2024**, *57*, 509.
[48] X. Guo, C. McCleese, C. Kolodziej, A. C. S. Samia, Y. Zhao, C. Burda, *Dalt. Trans.* **2016**, *45*, 3806.
[49] Y. Ren, B. Duan, Y. Xu, Y. Huang, Z. Li, L. Hu, T. Hayat, H. Wang, J. Zhu, S. Dai, *Sci. China Mater.* **2017**, *60*, 392.
[50] A. Bertoluzza, S. Bonora, M. A. Battaglia, P. Monti, *J. Raman Spectrosc.* **1979**, *8*, 231.